Title

Small form factor, flexible, dual-modality handheld probe for smartphone-based, point-of-care oral and oropharyngeal cancer screening.

Journal

Journal of biomedical optics, 24(10)

ISSN

1083-3668

Authors

Uthoff, Ross D
Song, Bofan
Sunny, Sumsum
et al.

Publication Date

2019-10-01

DOI

10.1117/1.jbo.24.10.106003

Peer reviewed

Journal of Biomedical Optics

BiomedicalOptics.SPIEDigitalLibrary.org

Small form factor, flexible, dual-modality handheld probe for smartphone-based, point-of-care oral and oropharyngeal cancer screening

Ross D. Uthoff
Bofan Song
Sumsum Sunny
Sanjana Patrick
Amritha Suresh
Trupti Kolur
Keerthi Gurushanth
Kimberly Wooten
Vishal Gupta
Mary E. Platek
Anurag K. Singh
Petra Wilder-Smith
Moni Abraham Kuriakose
Praveen Birur
Rongguang Liang

Ross D. Uthoff, Bofan Song, Sumsum Sunny, Sanjana Patrick, Amritha Suresh, Trupti Kolur, Keerthi Gurushanth, Kimberly Wooten, Vishal Gupta, Mary E. Platek, Anurag K. Singh, Petra Wilder-Smith, Moni Abraham Kuriakose, Praveen Birur, Rongguang Liang, "Small form factor, flexible, dual-modality handheld probe for smartphone-based, point-of-care oral and oropharyngeal cancer screening," *J. Biomed. Opt.* **24**(10), 106003 (2019), doi: 10.1117/1.JBO.24.10.106003.

SPIE.

Small form factor, flexible, dual-modality handheld probe for smartphone-based, point-of-care oral and oropharyngeal cancer screening

Ross D. Uthoff,[a,*,†] Bofan Song,[a,†] Sumsum Sunny,[b,c] Sanjana Patrick,[d] Amritha Suresh,[b,c] Trupti Kolur,[b] Keerthi Gurushanth,[e] Kimberly Wooten,[f] Vishal Gupta,[f] Mary E. Platek,[f,g] Anurag K. Singh,[f] Petra Wilder-Smith,[h] Moni Abraham Kuriakose,[b,c] Praveen Birur,[d,e] and Rongguang Liang[a,*]

[a]The University of Arizona, College of Optical Sciences, Tucson, Arizona, United States
[b]Mazumdar Shaw Medical Centre, Bangalore, Karnataka, India
[c]Mazumdar Shaw Medical Foundation, Bangalore, Karnataka, India
[d]Biocon Foundation, Bangalore, Karnataka, India
[e]KLES Institute of Dental Sciences, Bangalore, Karnataka, India
[f]Roswell Park Comprehensive Cancer Center, Buffalo, New York, United States
[g]D'Youville College, Buffalo, New York, United States
[h]University of California, Irvine, Beckman Laser Institute, Irvine, California, United States

Abstract. Oral cancer is a growing health issue in low- and middle-income countries due to betel quid, tobacco, and alcohol use and in younger populations of middle- and high-income communities due to the prevalence of human papillomavirus. The described point-of-care, smartphone-based intraoral probe enables autofluorescence imaging and polarized white light imaging in a compact geometry through the use of a USB-connected camera module. The small size and flexible imaging head improves on previous intraoral probe designs and allows imaging the cheek pockets, tonsils, and base of tongue, the areas of greatest risk for both causes of oral cancer. Cloud-based remote specialist and convolutional neural network clinical diagnosis allow for both remote community and home use. The device is characterized and preliminary field-testing data are shared. [DOI: 10.1117/1.JBO.24.10.106003]

Keywords: autofluorescence imaging; mobile health; oral cancer screening; biomedical imaging.

Paper 190247R received Jul. 17, 2019; accepted for publication Sep. 24, 2019; published online Oct. 22, 2019.

1 Introduction

Oral cancer incidence and death rates are an ongoing concern in low- and middle-income countries (LMICs). LMICs suffer the majority of worldwide new cancer cases and deaths along with <50% five-year survival rates in some locations.[1,2] The major risk factor for oral squamous cell carcinoma and oral submucous fibrosis in many LMICs is betel quid chewing, with or without the inclusion of tobacco.[3,4] Furthermore, oral and oropharyngeal cancers are increasing in younger populations (especially men) in middle- to high-income communities (MHICs) due to the spread of human papillomavirus (HPV), mostly affecting the tonsils and base of the tongue (BOT).[5–7]

Conventional oral examinations (COEs) provide a high specificity[8] for visible lesions. However, lesions can be at an advanced stage before they are visible. Additionally, with higher incidence rates deep in the oral cavity and in oropharyngeal regions, accessibility can be an issue for a COE. Autofluorescence imaging (AFI) has the potential to be an important oral and oropharyngeal cancer adjunctive screening tool to aid in discrimination of oral potentially malignant lesions not visible during a COE.[1] Previously, we described an AFI and white light imaging (WLI) smartphone-based oral cancer screening device with the ability to capture both whole cavity and intraoral images.[9] Following is an intraoral probe with improved form factor to increase clinician ergonomics and patient comfort while improving access to the BOT and oropharynx, significant cancer sites.[7,10]

2 Materials

We have developed a small form-factor, intraoral AFI, and polarized white light imaging (PWLI) handheld probe utilizing a commercially available camera module (OV5648, Omnivision, Santa Clara, California), connected by USB to an LG G4 smartphone (LG, Seoul, South Korea) for low-cost, point-of-care oral, and oropharyngeal cancer screening (Fig. 1).

The 3D-printed probe housing of VeroBlackPlus (Stratasys, Eden Prairie, Minnesota) provides mounting for the camera, camera printed circuit board (PCB), illumination LEDs, filters, polarizers, and wiring while also integrating a 25-mm-diameter handle and flexible section near the imaging head. The 135.5-mm usable probe length allows access to the BOT and oropharynx while the 14.4 mm × 8.4 mm probe cross-section maintains patient comfort during imaging tasks. Significantly, the 24-mm flexible silicone (Mold Star 20T and Black Silc Pig, Smooth-On, Macungie, Pennsylvania) section provides up to 470% elongation before break, bending up to 45 deg in either direction (Fig. 1) to better access all areas of the oral cavity. A 250-μm thick, 11-mm wide piece of aluminum sheet metal embedded in the flexible section is a ductile core to the silicone elastomer, maintaining the probe head angle after bending to the desired position. The aluminum sheet keeps the two sections of the

*Address all correspondence to Ross D. Uthoff, E-mail: rossuthoff@email.arizona.edu; Rongguang Liang, E-mail: rliang@optics.arizona.edu

†These authors contributed equally to this work

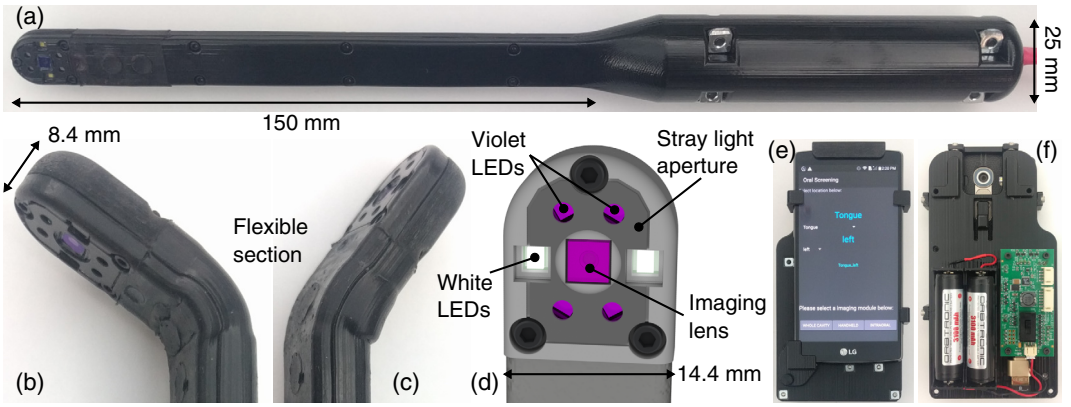

Fig. 1 Intraoral probe system view showing the handheld probe: (a) overall system size; (b), (c) the flexible head; (d) the imaging and LED illumination apertures, along with the (e) installed smartphone running the custom Android application and (f) installed electronics.

probe attached with notches to capture the screws joining the two halves of the probe head clamshell while also serving as a thermal sink for the illumination LEDs. To ensure the elastomer stretches with the probe as it is bent and does not pull away from the seams of the 3D-printed plastic/silicone interface (keeping the electronics from being exposed), the silicone overlaps the 3D-printed plastic a minimum of 5 mm and maximum of 11 mm on each end, and 750-μm vertical capture features in the plastic embed into the silicone. The interface is further reinforced with Dow Corning 700 (DowDuPont, Midland, Michigan) silicone adhesive. Creating the silicone section is the last assembly step; the 3D-printed mold is clamped around the two probe halves and the silicone injected through the vents. Opposing vents in the mold reduce air pockets in the final cured silicone shape. The various features and components of the aluminum stiffener, flexible section, and silicone mold are shown in Fig. 2.

Illumination for PWLI and AFI is accomplished with two white (4000 K) and four violet (400 nm) LEDs (Lumileds, Amsterdam, Netherlands), respectively. The LEDs are mounted on an annulus of flexible, polyimide PCB, surrounding the camera module in a plane-symmetric pattern to maximize illumination uniformity without the use of additional optical components. The PCB is filled with large copper planes to increase heat transfer while the backside copper is exposed and attached to the aluminum stiffener with an electrically insulating, thermally conductive epoxy (DP240, 3M, St. Paul, Minnesota). To enable AFI, a 425-nm shortpass excitation filter (Asahi Spectra, Tokyo, Japan) is installed in front of the violet LEDs and a complementary 470-nm longpass emission filter (Asahi Spectra) is installed in front of the camera module.

The fixed emission filter in the imaging channel distorts the color space during WLI and is corrected by applying the transformation matrix calculated using a standard 24-color color checker (X-Rite, Grand Rapids, Michigan).

$$\mathbf{A} = \begin{vmatrix} 0.6198 & 0.0568 & -0.0957 \\ -0.0872 & 0.9391 & -0.1073 \\ 0.0692 & 0.3618 & 0.0699 \end{vmatrix}. \quad (1)$$

The stray light aperture prevents unfiltered scatter from the edges of the excitation filter to reach the tissue plane. Orthogonal linear polarizers (Edmund Optics, Barrington, New Jersey) in front of the white LEDs and the camera module enable

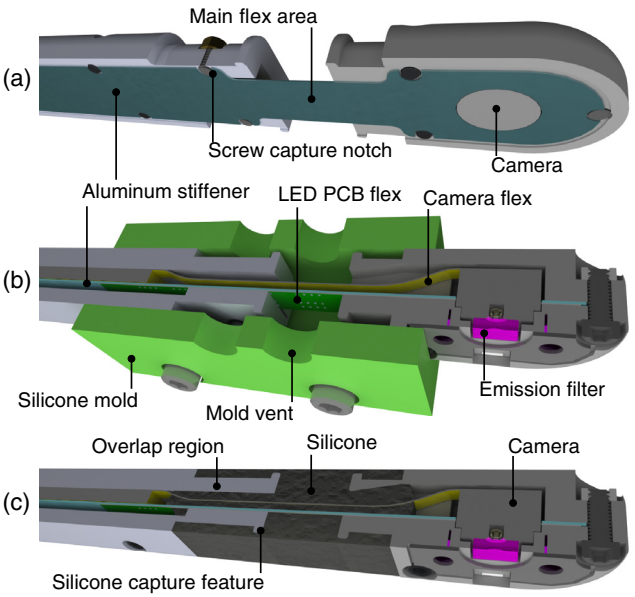

Fig. 2 Cross-section images of the system mechanical design highlighting features related to the flexible silicone section. (a) A horizontal section view up to the aluminum stiffener/heatsink (rendered in teal for visibility) demonstrating its shape and position in the probe head. The stiffener is clamped between the two halves of the probe head and, along with the screw capture notches, keeps the two sections of the probe rigidly connected. (b) A vertical section view of the final assembly step, where the green-colored mold for the silicone is clamped around the probe head. The camera PCB and illumination LED PCB flex cables span the flexible section. The LED flex PCB surrounds the camera and is attached to the heatsink with electrically insulating epoxy. (c) A vertical section view of the device after the silicone has been injected into the mold and cured. Here, the silicone and plastic overlap region along with the capture features is visible. The capture features and overlap increase robustness in the joint. After curing, the mold is removed and the silicone/3D-printed plastic interface is reinforced with silicone adhesive.

PWLI. The thermally sensitive film polarizer is positioned at a distance from the LED emission surface by a 1-mm-thick PMMA window.

The USB-connected camera module integrates an image sensor (5 MP, 3673.6 μm $\times$ 2738.4 μm), $\simeq$4.1 mm focal length imaging lens, and control circuitry on a rigid-flex PCB with the image sensor and lens mounted on the end of the 30-mm-long

flexible cable. The long flex PCB cable is embedded in the silicone section of the probe, with the rigid portion of the PCB containing driving and readout circuitry in the nonmoving section. The vendor-supplied lens focal length is calculated from the maximum chief ray angle (29 deg) and the sensor diagonal (4.6 mm) provided in the sensor module datasheet. The lens is installed in a threaded barrel and the position adjusted to provide a working distance of 20 mm, providing a cropped field of view (FOV) of 15 mm × 20 mm.

The probe is compatible with the previously reported 3D-printed structure for mounting of the smartphone, LED driving electronics, and whole-cavity imaging module.[9] Additionally, the system maintains the custom Android application for image capture, processing algorithms, cloud server data upload, convolutional neural network (CNN) classification, and web browser remote diagnosis features of the previously reported system.[9,11]

During patient testing, the probe is covered with a hygienic sleeve (TIDI Products, Neenah, Wisconsin).

3 Methods

To characterize the imaging system performance, the FOV and cutoff frequency were measured by imaging a 1951 USAF resolution test chart, and a slanted edge test[12,13] was used to compare the actual on-axis modulation transfer function (MTF) to the theoretical calculated from the image sensor pixel pitch and lens magnification.

Uniformity and leakage were evaluated to benchmark the illumination system. Illumination uniformity was quantified using the coefficient of variation

$$\text{uniformity} = 1 - c_v = 1 - \frac{\sigma}{\bar{x}}, \tag{2}$$

where σ is the standard deviation and $\bar{x}$ is the mean of the gray-scale pixel values when imaging a 50% neutral value matte card (Munsell, Grand Rapids, Michigan). Illumination leakage was measured by imaging a mirror under violet illumination and measuring the returned signal on each color channel relative to the maximum possible signal for the channel

$$\text{leakage} = \frac{\sum_{i=0}^{N-1} x_i}{255N}, \tag{3}$$

where x_i is the pixel value and N is the number of pixel in the channel.

The maximum permissible exposure (MPE) of the AFI and PWLI illumination was calculated according to the International Electrotechnical Commission 60825-1:2014.[14] Since the AFI LED bandwidth has power in two wavelength regions (315 to 400 nm and 400 to 700 nm), the most stringent limit is applied. With an exposure time of 0.8 s, MPE is calculated as

$$\text{MPE} = C_1\ \text{J m}^{-2} = 5.6 \times 10^3\, t^{0.25}\ \text{J m}^{-2} = 5296\ \text{J m}^{-2}. \tag{4}$$

With the following assumptions (a) LED power run at 90% of maximum 675 mW, (b) emission area of 1 mm^2, (c) emission duration of 800 ms, (d) Lambertian emission, (e) the closest tissues could be to the emission plane is 1.5 mm, and (f) skin aperture diameter is 3.5 mm. The flux transfer from an LED to tissue given the correct configuration factor is[15]

$$\Phi_{\text{tissue}} = \Phi_{\text{LED}} F = \Phi_{\text{LED}} \frac{1}{2}\left[X - \left(X^2 - 4\frac{R_2^2}{R_1^2}\right)^{\frac{1}{2}}\right] = 0.0065\ \text{W}, \tag{5}$$

where $R_1 = r_1/d$, the radius of the emitter divided by the distance between the two planes; $R_2 = r_2/d$, the radius of the tissue plane divided by the distance between the two planes; and $X = 1 + (1 + R_2^2)/R_1^2$, corresponding to an exposure of 541 Jm^{-2}, safely below the MPE. The white LEDs output is also below the MPE as they have a similar exposure to the violet LEDs but are run at 10% of maximum power and have a higher limit due to the wavelength band.

A pilot human subjects study is currently being performed to demonstrate the capability of the hardware to reach oral and oropharyngeal sites and the feasibility of using CNN classification algorithms. This study is institutional review board approved by Mazumdar Shaw Cancer Centre (NNH/MEC-CL-2016-394), University of California, Irvine (HS#2002-2805), and Rowsell Park Comprehensive Cancer Center (I 49117). For this study, all subjects provided informed written and oral consent before testing. The workflow for testing the handheld probe was reported previously.[9] The patients first have a conventional oral exam, and then the smartphone-based exam is administered. WLI and PWLI are collected with the whole cavity module[9] and with the handheld probe. With the probe, both the lesion area and the normal contralateral area are imaged to provide additional data for the CNN. After testing, the images are uploaded either to an internal electronic health record system or to the cloud for remote specialist review and classification by the CNN.

To provide further visual information to the diagnosing specialist, additional images are created from the AFI. Fluorescence loss can be visualized from a luminance map where the green channel mean is subtracted from the green channel

$$\mathbf{f} = \mathbf{I_G} - \bar{\mathbf{I}}_{\mathbf{G}}, \tag{6}$$

and a red/green ratio map[16,17]

$$\mathbf{f} = \frac{\mathbf{I_R}}{\mathbf{I_G}} \tag{7}$$

can signal additional areas of concern. The CNN uses both the relative green luminance information and the red/green ratio in its analysis.

4 Results

Figure 3 shows the FOV of the system and a zoomed view to show group 4–3 of the resolution target is resolvable, a spatial frequency of 20.16 lp/mm. This result matches the calculated MTF from the slanted edge test in Fig. 3, where the estimated cutoff frequency of 25 lp/mm results in a calculated image space numerical aperture of NA = 0.007. The resulting depth of field is[18]

$$\frac{L_o f D}{fD - L_o B} - \frac{L_o f D}{fD + L_o B} \simeq 12.5\ \text{mm}, \tag{8}$$

where L_o is the nominal object plane (−20 mm), f is the focal length of the lens (4.1 mm), D is the entrance pupil diameter (0.073 mm), and B is the blur diameter chosen to be three pixels (4.2 μm).

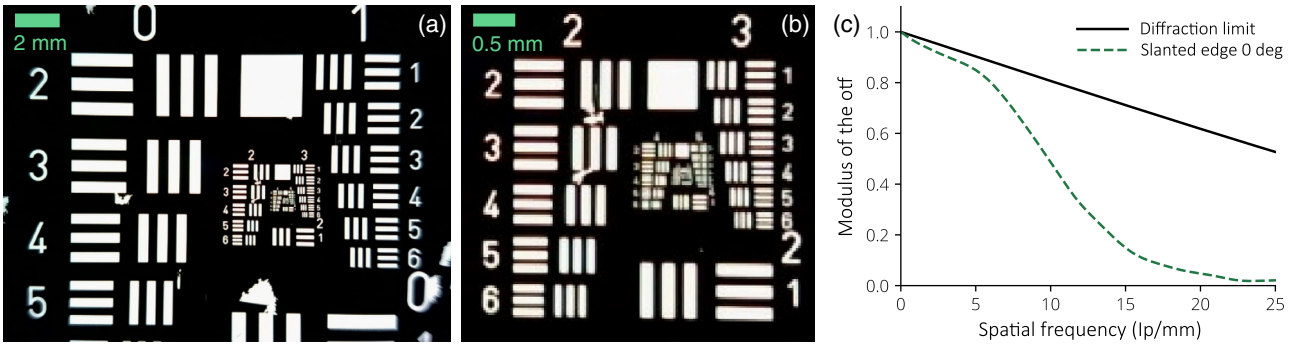

Fig. 3 Image of a 1951 USAF resolution test chart showing (a) the 15 mm × 20 mm FOV and (b) contrast limit. The zoomed contrast limit image (b) shows group 4–3 is resolvable, a cutoff frequency of 20.16 lp/mm. (c) A comparison of the theoretical diffraction limit and measured on-axis MTF performance.

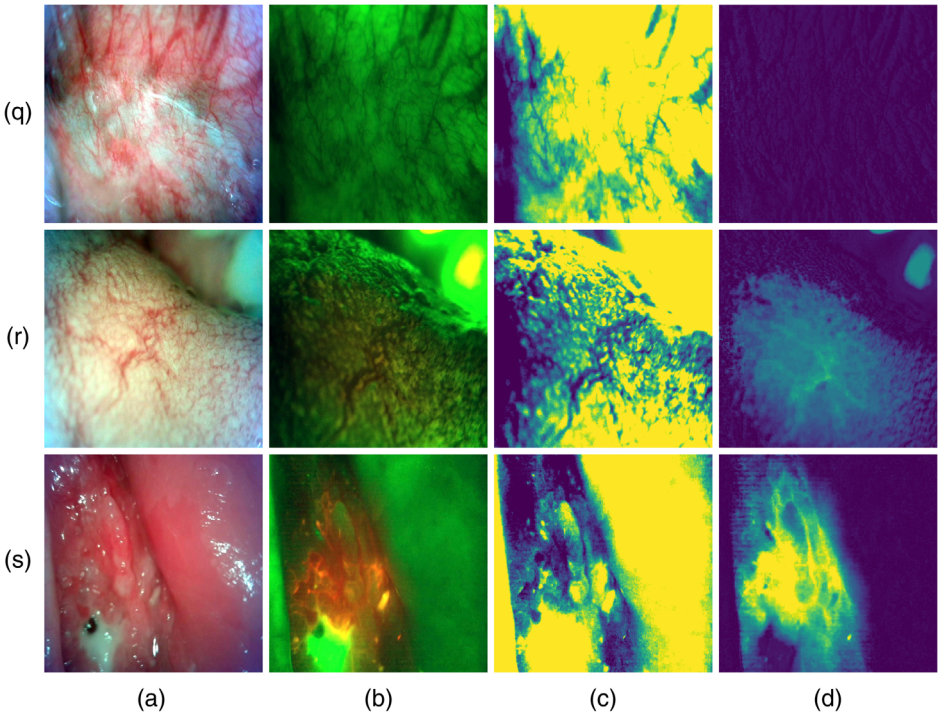

Fig. 4 Sample (column a) white light, (column b) autofluorescence, (column c) green luminance subtraction, and (column d) red/green ratio handheld intraoral images with clinical diagnoses of (q) normal/variation, location: floor of the mouth; (r) normal/variation, location: tongue; and (s) OSCC, location: right buccal mucosa.

Illumination uniformity was measured to be 83.80% for white light illumination and 89.84% for violet light illumination. Leakage was measured as 14.01%, 13.00%, and 28.97% for the red, green, and blue channels, respectively.

Oral and oropharyngeal images demonstrating the ability of the handheld probe to capture AFI and PWLI at the BOT and oropharynx with the maps created from Eqs. (6) and (7) are shown in Figs. 4 and 5. Figure 4 shows AFI and PWLI along with the maps created from Eqs. (6) and (7) for normal and OSCC clinical diagnoses. Figure 5 demonstrates the ability to capture AFI and PWLI at the BOT and oropharynx, areas of increased cancer risk from HPV. For these sets of images, the upper limit of the dynamic range of the fluorescence loss images of column c in Figs. 4 and 5 has been deliberately limited for better visualization of low fluorescence (low luminance) regions. Regions of high luminance in the red-to-green ratio images of column d indicate possible cancerous conditions. The pixelated regions in the corners of some of the red-to-green ratio images are artifacts of small number division.

5 Discussion

AFI with excitation at ≃405 nm[19,20] along with PWLI is a promising modality for low-cost, low-complexity devices to increase detection rates and provide earlier detection of oral and oropharyngeal cancer.[21] Here, decreased fluorescence signal at ≃500 nm indicates increasing dysplasia while increased signal at ≃635 nm can serve as an additional indicator.[1] The necessary excitation wavelengths now have readily available LED sources

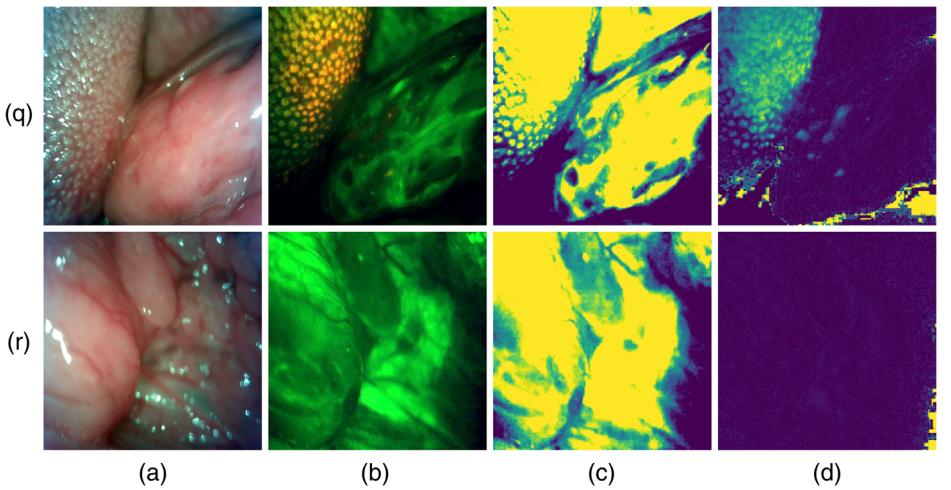

Fig. 5 Sample (column a) white light, (column b) autofluorescence, (column c) green luminance subtraction, and (column d) red/green ratio handheld intraoral images demonstrating the ability to image the BOT.

at increasingly lower cost and the resulting autofluorescence emission spectrum peaks are easily detectable by a smartphone camera.

This new intraoral probe provides marked improvements in geometry to increase access to the significant oral and oropharyngeal cancer sites compared to other AFI devices. Table 1 highlights the differences in form-factor, features, and capabilities between this intraoral probe, our previous device,[9] and two commercially available AFI devices, the VELscope™[22] (Apteryx Imaging, Akron, Ohio) and the Identifi®[23] (StarDental, Lancaster, Pennsylvania).

The new probe has increased its usable intraoral length by ≃20 mm over our previous device while decreasing the maximum cross-sectional area by over 80%. Removing the requirement to use the smartphone camera for imaging enables a smaller and lighter system by eliminating the design constraints, bulk, and cost of a long-track-length, well-aligned optical system. These geometry differences are visualized in Fig. 6. The drastic reduction in cross-sectional area along with the flexible joint enables better accommodation of the oral cavity's and oropharynx's contours, leading to the consistent ability to image the BOT and tonsils. The previous device's length and size were insufficient to reach the BOT, and its inflexible imaging head was unable to orient for imaging the tonsils. While the VELscope™ is not an intraoral device, its geometry and long working distance does allow for imaging some oropharyngeal

Table 1 Comparison of AFI device features and specifications.

Parameter	This work	Uthoff 2018[9]	VELscope™	Identifi®
Usable intraoral length	135.5 mm	116.6 mm	Not intraoral	Similar to this work
Minimum intraoral cross-sectional area	113.1 mm^2	369.5 mm^2	Not intraoral	Similar to this work
Maximum intraoral cross-sectional area	116.5 mm^2	594.0 mm^2	Not intraoral	Similar to this work
Working distance	20 mm	10 mm	80 mm	No camera
Depth of field	12.5 mm	0.6 mm	>20 mm	No camera
FOV area	300 mm^2	247 mm^2	1257 mm^2	No camera
Flexible joint	Yes	No	Not intraoral	Mirror
Accesses BOT	Yes	No	No	Maybe
Accesses tonsils and posterior pharynx	Yes	No	Yes	Maybe
Native image capture, processing, transmission	Yes	Yes	W/peripheral	No
AFI	Yes	Yes	Yes	Yes
PWLI	Yes	WLI	No	WLI
Green-amber imaging	No	No	No	Yes

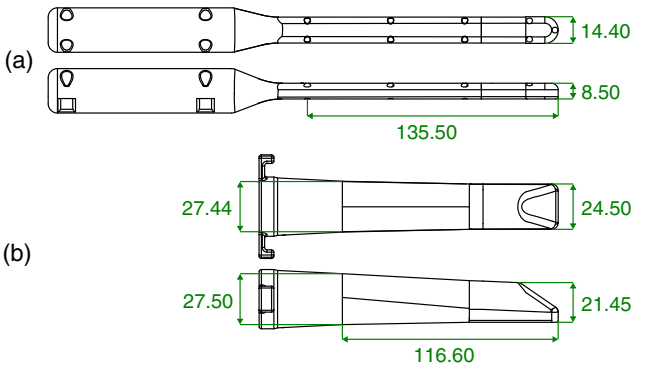

Fig. 6 Comparison of mechanical outlines for (a) the probe proposed in this paper and (b) the previously published probe[9] demonstrating its greatly reduced intraoral dimensions.

sites (tonsils, posterior pharynx) but cannot access the BOT. From images, the size of the Identifi® is estimated to be similar to this work's probe.

The illumination uniformity is decreased compared to the previous probe due to fewer LED sources but still maintains a high uniformity approaching 90%. Leakage data were only available for the current device measuring under 15% for both the red and green channels, the channels of interest (the blue channel is discarded), an area for improvement.

This probe's depth of field is increased by 22× compared to the previous probe while maintaining sufficient resolution to resolve vasculature as seen in Fig. 4. The VELscope™ similarly benefits from a long depth of field whereas the previous probe's short depth of field led to >50% of the images with too much blur to analyze in our first pilot study.[9] Importantly, the FOV is increased, increasing the ability of a remote clinician to orient themselves in the image, valuable feedback from testing the previous probe. The VELscope™ and Identifi® both offer a larger FOV (due to not being intraoral and due to not implementing a camera, respectively) than this probe but the downsides are the VELscope™ not being able to access the BOT and the Identifi® lacking native image capture outweigh this smaller FOV.

The new probe integrates a full feature set of AFI, PWLI (decreasing the area of images saturated from specular reflection), and native image capture, processing, and transmission, lacking only the green-amber illumination of the Identifi®, giving it a high size-to-feature ratio compared to the other devices. Additionally, the new form-factor is derived from commercially successful intraoral imaging devices, such as the CS1500 (Carestream Dental, Atlanta, Georgia) and Claris i5HD (SOTA Imaging, Orange, California), suggesting improved ergonomics for both the clinician and patient.

Table 2 Prescription for imaging lens with increased FOV and resolution.

Surface	Material	Radius	Thickness	Conic	α_2
Object	Air	—	15.000	—	—
Stop	OKP4HT	−2.520	0.3	—	−0.129
3	E48R	0.833	0.6	—	—
4	Air	−0.739	2.684	0.430	0.157
Image	—	—	—	—	—

Future improvements should include decreasing leakage from the AFI illumination. Additional improvements could include a custom designed lens system to increase the FOV and optimization of the working distance based on doctor use and patient comfort feedback. A sample optical design meeting these criteria is shown in Fig. 7 with the optical prescription provided in Table 2. Here, the angular full FOV has been in increased to 120 deg along the diagonal, resulting in a spatial FOV of 45.3 mm × 33.7 mm with increased optical performance as measured by MTF compared to the USB camera lens. The increased FOV would allow remote specialists to more easily orient themselves when analyzing images outside of the clinical setting. The design utilizes a single achromat with an object space NA = 0.0035, image space NA = 0.023, providing a 9.4-mm depth of field where the focal length $f = 1.875$ mm and the entrance pupil diameter $D = 0.165$mm. This large depth of field is critical for reducing the number of out-of-focus images from hand movement during image capture.

The sag of the aspheric surfaces is defined by[24]

$$z = \frac{cr^2}{1 + \sqrt{1 - (1 + k)c^2r^2}} + \alpha_2 r^4, \tag{9}$$

where r is the radial distance from the optical axis, c is the surface curvature $(1/R)$, k is the conic constant, and α_n defines the polynomial coefficients. Specifying plastic lenses (OKP4HT, Osaka Gas Chemicals, Osaka, Japan; E48R, Zeon, Tokyo, Japan) allows for molding technologies to achieve low-cost parts even with aspheric surfaces.

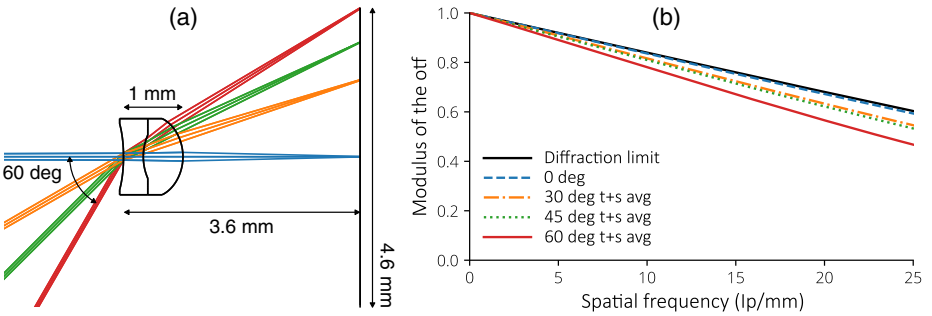

Fig. 7 Optical design for a 120-deg full FOV, image space NA = 0.023 lens with increased MTF performance compared to Fig 3. (a) The layout of the optical design with dimensions; (b) provides the theoretical MTF performance.

With the small camera modules, there is opportunity to include two camera modules in the head, one camera with a wide FOV, low NA lens and the other with a high NA lens and narrow FOV, providing wide FOV imaging and high-resolution imaging at the same time. For high-resolution imaging, a camera module with autofocus capability would be preferred. Alternatively, the same lens could be used for both cameras to enable 3-D spectroscopic imaging.

Additionally, the ability to 3D-print the flexible area along with the plastic would greatly decrease assembly time. This was attempted with Stratasys Tango material along with VeroBlackPlus but the Tango's elongation at break of only ≃200% was not sufficient as the interface tore after only a few bending cycles. New 3D-printing materials could enable this change in the future.

Lastly, with an exposure time of 250 ms, motion of the probe during image capture affects quality. Usability could be improved by the addition of a camera control button on the probe handle so the clinician could prompt image capture from the probe, as well as the smartphone. In addition, since the LEDs are run at 10% of the emission limit, an increase in LED power and a corresponding decrease in camera exposure time would further limit blur in the images.

6 Conclusion

We have demonstrated a compact, dual-modality imaging device with a flexible head to enable good quality AFI and PWLI in oral (cheek pockets) and oropharyngeal (tonsils and BOT) areas with high cancer incidence rates from betel quid chewing and HPV but more difficult to access with conventional aided or unaided visual examinations, leading to earlier detection and diagnosis of precancerous or cancerous conditions. Advances in high-power, low-cost light sources, 3D-printing, and low-cost smartphones are instrumental to the creation of simple AFI and PWLI prototype devices for oral and oropharyngeal cancer screening in LMICs and MHICs. USB-connected cameras remove design constraints related to using the smartphone's camera allowing better ergonomics for the clinician and increased comfort for the patient, a system better able to address the imaging need while keeping the desirable functions and portability of the smartphone.

7 Supplementary Material

The design files for the LED driver have been released on GitHub under the GPL-3.0 license.[25,26]

Disclosures

The authors have declared that no competing interests exist.

Acknowledgments

We are grateful for our funding sources. This research was supported by the National Institute of Biomedical Imaging and Bioengineering of the U.S. National Institutes of Health (NIH) under Award No. UH2EB022623 and NIH Award No. 1S10OD018061-01A1. Uthoff received funding from the National Institutes of Health, National Institute of Biomedical Imaging and Bioengineering, Graduate Training in Biomedical Imaging and Spectroscopy Grant No. T32EB000809. We would like to thank Pier Morgan and the Center for Gamma-Ray Imaging (CGRI) for assistance with the rapid prototype printer, Ken Almonte for guidance on the LED driver design, and David Coombs for PCB assembly assistance.

References

1. X. Luo et al., "Accuracy of autofluorescence in diagnosing oral squamous cell carcinoma and oral potentially malignant disorders: a comparative study with aero-digestive lesions," *Sci. Rep.* **6**, 29943 (2016).
2. J. Ferlay et al., "Cancer incidence and mortality worldwide: sources, methods and major patterns in GLOBOCAN 2012: Globocan 2012," *Int. J. Cancer* **136**(5), E359–E386 (2015).
3. H. K. Amarasinghe et al., "Betel-quid chewing with or without tobacco is a major risk factor for oral potentially malignant disorders in Sri Lanka: a case-control study," *Oral Oncol.* **46**(4), 297–301 (2010).
4. H. Song et al., "Betel quid chewing without tobacco: a meta-analysis of carcinogenic and precarcinogenic effects," *Asia Pac. J. Public Health* **27**(2), NP47–NP57 (2015).
5. D. Young et al., "Increase in head and neck cancer in younger patients due to human papillomavirus (HPV)," *Oral Oncol.* **51**(8), 727–730 (2015).
6. M. L. Gillison et al., "Epidemiology of human papillomavirus-positive head and neck squamous cell carcinoma," *J. Clin. Oncol.* **33**(29), 3235–3242 (2015).
7. T. Ramqvist et al., "Human papillomavirus and tonsillar and base of tongue cancer," *Viruses* **7**(3), 1332–1343 (2015).
8. R. Sankaranarayanan et al., "Effect of screening on oral cancer mortality in Kerala, India: a cluster-randomised controlled trial," *Lancet* **365**(9475), 1927–1933 (2005).
9. R. D. Uthoff et al., "Point-of-care, smartphone-based, dual-modality, dual-view, oral cancer screening device with neural network classification for low-resource communities," *PloS One*, **13**(12), e0207493 (2018).
10. A. K. Agarwal et al., "Treatment delay in oral and oropharyngeal cancer in our population: the role of socio-economic factors and health-seeking behaviour," *Indian J. Otolaryngol. Head Neck Surg.* **63**(2), 145–150 (2011).
11. B. Song et al., "Automatic classification of dual-modality, smartphone-based oral dysplasia and malignancy images using deep learning," *Biomed. Opt. Express* **9**(11), 5318–5329 (2018).
12. P. D. Burns, "Slanted-edge MTF for digital camera and scanner analysis," in *Proc. IS&T*, pp. 135–138 (2000).
13. P. D. Burns, "Sfrmat3: SFR analysis for digital cameras and scanners," *LosBurns Imaging Software*, 2009, http://www.losburns.com/imaging/software/SFRedge/index.htm.
14. International Electrotechnical Commission et al., *IEC 60825–1; International Standard: Safety of Laser Products—Part 1: Equipment Classification and Requirements*, 3.0 ed., IEC, Geneva, Switzerland (2014).
15. A. Arecchi et al., *Field Guide to Illumination*, SPIE Press, Bellingham, Washington (2007).
16. R. J. Mallia et al., "Laser-induced autofluorescence spectral ratio reference standard for early discrimination of oral cancer," *Cancer* **112**(7), 1503–1512 (2008).
17. A. Zuluaga et al., "Fluorescence excitation emission matrices of human tissue: a system for in vivo measurement and method of data analysis," *Appl. Spectrosc.* **53**(3), 302–311 (1999).
18. J. E. Greivenkamp, *Field Guide to Geometrical Optics, Number v. FG01 in SPIE Field Guides*, SPIE Press, Bellingham, Washington (2004).
19. D. L. Heintzelman et al., "Optimal excitation wavelengths for in vivo detection of oral neoplasia using fluorescence spectroscopy," *J. Photochem. Photobiol.* **72**(1), 103–113 (2000).
20. D. Roblyer et al., "Objective detection and delineation of oral neoplasia using autofluorescence imaging," *Cancer Prev. Res.* **2**(5), 423–431 (2009).
21. A. Rashid et al., "The use of light-based (optical) detection systems as adjuncts in the detection of oral cancer and oral potentially malignant disorders: a systematic review," *J. Oral Pathol. Med.* **44**(5), 307–328 (2015).
22. Apteryx Imaging, "VELscope Vx system," 2019, https://apteryx.com/product/velscope-vx-system/.
23. DentalEZ, "Identifi: oral mucosal visual enhancement system," 2019, http://www.identafi.net/.
24. R. Kingslake et al., *Lens Design Fundamentals*, Academic Press, London (2009).

25. R. D. Uthoff, "Rossuthoff/multichannel_led_driver: KiCAD design files," *GitHub* (2018).
26. R. D. Uthoff, "Rossuthoff/kicad_footprints: custom footprints for pcb designs," *GitHub* (2018).

Ross D. Uthoff is a PhD candidate at the University of Arizona, James C. Wyant College of Optical Sciences. He received his BS degree in optical engineering from Rose-Hulman Institute of Technology. His research interest is optical system design, currently being applied to medical imaging using smartphones. He is a member of SPIE.

Biographies of the other authors are not available.